ADVANCED MATERIALS
www.advmat.de

A Switchable One-Compound Diode

Anna Vogel, Alfred Rabenbauer, Philipp Deng, Ruben Steib, Thorben Böger, Wolfgang G. Zeier, Renée Siegel, Jürgen Senker, Dominik Daisenberger, Katharina Nisi, Alexander W. Holleitner, Janio Venturini, and Tom Nilges**

A diode requires the combination of p- and n-type semiconductors or at least the defined formation of such areas within a given compound. This is a prerequisite for any IT application, energy conversion technology, and electronic semiconductor devices. Since the discovery of the pnp-switchable compound $Ag_{10}Te_4Br_3$ in 2009, it is in principle possible to fabricate a diode from a single material without adjusting the semiconduction type by a defined doping level. Often a structural phase transition accompanied by a dynamic change of charge carriers or a charge density wave within certain substructures are responsible for this effect. Unfortunately, the high pnp-switching temperature between 364 and 580 K hinders the application of this phenomenon in convenient devices. This effect is far removed from a suitable operation temperature at ambient conditions. $Ag_{18}Cu_3Te_{11}Cl_3$ is a room temperature pnp-switching material and the first single-material position-independent diode. It shows the highest ever reported Seebeck coefficient drop that takes place within a few Kelvin. Combined with its low thermal conductivity, it offers great application potential within an accessible and applicable temperature window. $Ag_{18}Cu_3Te_{11}Cl_3$ and pnp-switching materials have the potential for applications and processes where diodes, transistors, or any defined charge separation with junction formation are utilized.

1. Introduction

The pn-junction is the most elementary building block of semiconducting devices, being found in diodes, transistors, sensors, and solar cells, to name a few. Currently, two different materials with opposite majority carriers are used to create a pn-junction. Nevertheless, some selected materials have previously been shown to switch between p- and n-conduction due to variations in temperature. In this context, the utilization of a single-material, thermally-controlled pn-junction would allow direct control of the character of these semiconducting devices including the position of the junction or its properties. Today, four different semiconducting materials are known to be capable of changing the mechanism of charge carrier transport between p- and n-type conduction. The first reported compound was $Ag_{10}Te_4Br_3$.[1–3] This material switches reversibly between p-type to n-type conduction at T_{pnp} = 390 K during an order-disorder phase transition of the cation substructure, driven by a charge density wave within the telluride substructure. Upon further heating or cooling down below the phase transition temperature the material switches back from n-type to p-type conduction. Later, $AgBiSe_2$ (T_{pnp} = 580 K), AgCuS (T_{pnp} = 364 K), and $Tl_2Ag_{12}Se_7$ (T_{pnp} = 410 K) were also discovered to show a comparable pnp-switch at elevated temperatures.[4–6] In all reported cases, the interplay of a highly

A. Vogel, A. Rabenbauer, P. Deng, R. Steib, J. Venturini, T. Nilges
School of Natural Sciences (NAT)
Department of Chemistry
Synthesis and Characterization of Innovative Materials group
Technical University of Munich
Lichtenbergstraße 4, 85748 Garching b. München, Germany
E-mail: janio.venturini@tum.de; tom.nilges@tum.de

T. Böger, W. G. Zeier
Institute of Inorganic and Analytical Chemistry
University of Münster
Corrensstraße 28/30, 48149 Münster, Germany

The ORCID identification number(s) for the author(s) of this article can be found under https://doi.org/10.1002/adma.202208698.

DOI: 10.1002/adma.202208698

T. Böger
International Graduate School for Battery Chemistry, Characterization, Analysis, Recycling and Application (BACCARA)
University of Münster
Corrensstraße 40, 48149 Münster, Germany

R. Siegel, J. Senker
Inorganic Chemistry III
University of Bayreuth
Universitätsstraße 30, 95447 Bayreuth, Germany

D. Daisenberger
Diamond Light Source
Harwell Science and Innovation Campus
Didcot, Oxfordshire OX11 ODE, UK

K. Nisi, A. W. Holleitner
Walter Schottky Institute and Physics Department
TU Munich, Am Coulombwall 4a, 85748 Garching b. München, Germany

dynamic substructure and the rearrangement of complementary structural units causes a modulation of the entire defect configuration and a switch of the semiconducting mechanism. A common building principle of all known pnp-switching materials is that they contain mobile d^{10} ions and a chalcogenide substructure, which interact with each other in a synergistic manner. Following this concept, the utilization of pn-switching materials in applications requires energy-friendly access to the switch close to the application temperature. Here, we report on a silver chalcogenide halide where the pn switch can be operated at room temperature without a huge and complex energy demand.

2. Results and Discussion

2.1. Structure Chemistry of $Ag_{18}Cu_3Te_{11}Cl_3$

Our group has recently prepared a material that shows pnp-switching close to room temperature: $Ag_{18}Cu_3Te_{11}Cl_3$. The crystal structures of the relevant polymorphs of this compound were determined from single crystals by temperature-dependent X-ray diffraction measurements (XRD). The structures can be described by a simple topological approach where neighboring anions are connected in such a way that different layers are realized: a Te 6^3 honeycomb net, a Cl 6.3.6.3 kagomé net, and a distorted Te 6.3.6.3 kagomé net (see **Figure 1**a). The layers are stacked along one crystallographic axis in the following sequence: Te 6^3 – Cl 6.3.6.3 – Te 6^3 – Te 6.3.6.3. While the Te 6^3 and the Cl 6.3.6.3 nets consist only of isolated Te^{2-} or Cl^- ions, the distorted Te 6.3.6.3 net is composed of $[Te_2]^{2-}$ dumbbells and additional coordinating Te^{2-} ions (see Figure 1b). More details concerning the structure are denoted in Figure S1 (Supporting Information). A similar Te 6.3.6.3 layer can also be found in the mineral stützite ($Ag_{55-x}Te_3$, Figure S2, Supporting Information).[7] Another feature of the anion substructure is the polyanionic Te_4 unit that vertically interpenetrates the Te 6^3 and Cl 6.3.6.3 nets. These units consist of a covalently-bonded $[Te_2]^{2-}$ dumbbell and two linearly

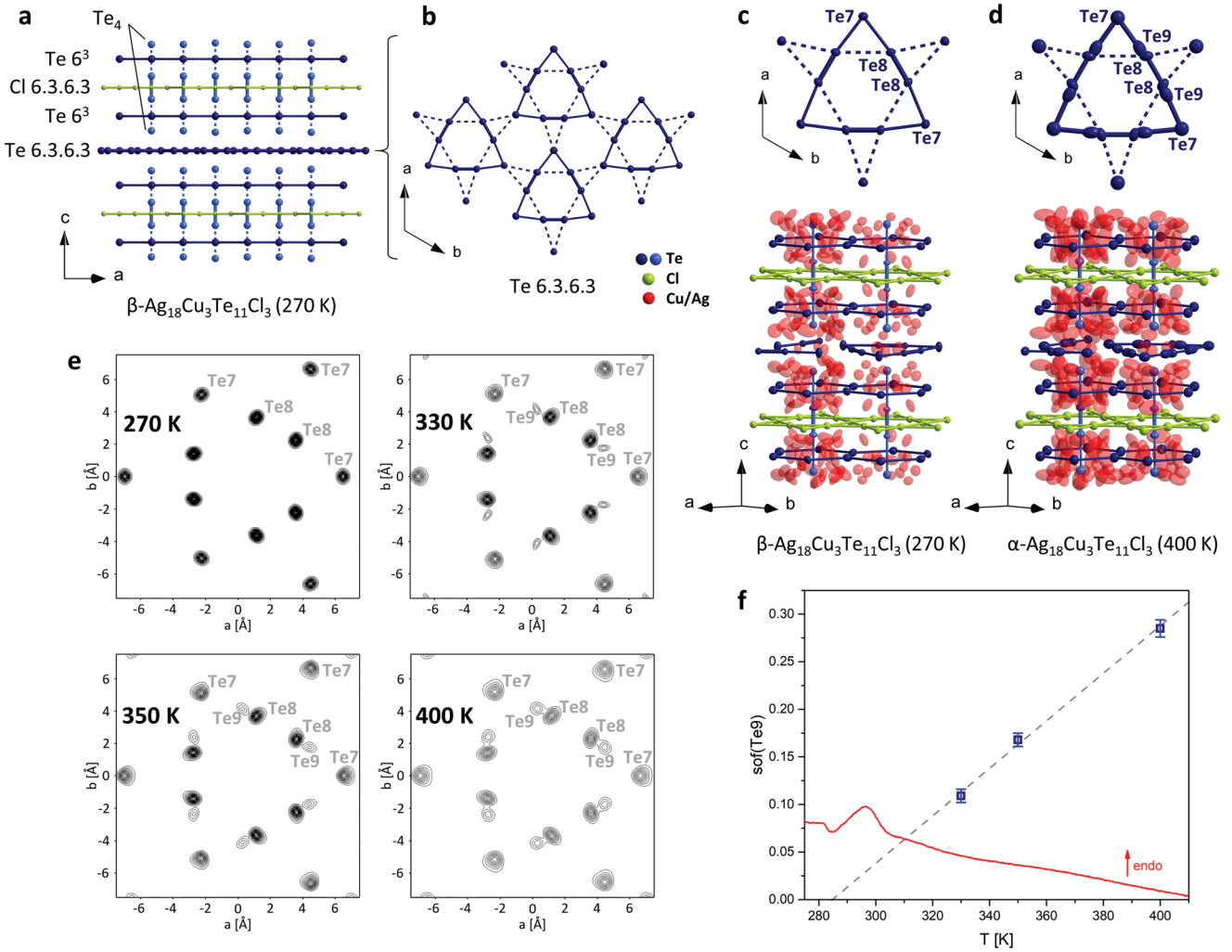

Figure 1. a) Scheme of anion substructure of β-$Ag_{18}Cu_3Te_{11}Cl_3$. b) Distorted Te 6.3.6.3 net. c,d) Structure sections of β- and α-$Ag_{18}Cu_3Te_{11}Cl_3$. Te nets are drawn in dark blue and Te_4 units in light blue for better differentiation. Displacement parameters are drawn at 70% probability. e) Joint probability density function (jpdf) images of sections of the Te 6.3.6.3 net at 270, 330, 350, and 400 K. One contour line represents 0.3 e $Å^{-3}$. f) Site occupancy factors (sof) of Te9 plotted against temperature (blue), linear fit (grey), and DSC (red).

coordinating Te^{2-} ions. The latter are located at distances closer than twice the van der Waals radius of tellurium (d_{vdW}(Te) = 2.06 Å),[8] illustrating a certain attractive bonding interaction. All other anions are well-separated from each other without showing any kind of bonding interaction. Similar Te_4 units can be found in $Ag_{10}Te_4Br_3$, the first ever described pnp-switching material (see Figures S2 and S3, Supporting Information).[1–3] The anion substructure of $Ag_{10}Te_4Br_3$ is closely related to that of $Ag_{18}Cu_3Te_{11}Cl_3$ – stacked Te 6^3 and Br 6.3.6.3 nets with interpenetrating Te_4 units – but the mechanisms of pnp-switching that will be discussed in the following are utterly different. The mobile and highly disordered d^{10} cations in $Ag_{18}Cu_3Te_{11}Cl_3$ are distributed in a liquid-like manner within the Te substructure (see Figure 1c,d) while the Cl 6.3.6.3 net acts as a separator for the mobile d^{10} ions. No silver or copper cations are distributed or located within this layer. All cation positions (red spheres in Figure 1c,d) in $Ag_{18}Cu_3Te_{11}Cl_3$ are mixed (by variable amounts of Cu^+ and Ag^+) and partially occupied. $Ag_{18}Cu_3Te_{11}Cl_3$ exhibits a high 2D ion mobility parallel to the (001) layer. This feature is substantiated by solid-state nuclear magnetic resonance (NMR) spectroscopy (as shown in Figure 4). Structural similarities to the mineral stützite and other coinage metal chalcogenide halides, like previously published $Cu_{20}Te_{11}Cl_3$, $Cu_{9.1}Te_4Cl_3$, and $Ag_{10}Te_4Br_3$, are discussed in the Supporting Information (shown in Figures S1 and S2, Supporting Information).[1–3,7,9,10]

2.2. Polymorphism

$Ag_{18}Cu_3Te_{11}Cl_3$ is a polymorphic compound that shows two reversible order-disorder phase transitions at 216(3) and 288(3) K (onset values from differential scanning calorimetry (DSC), **Figure 2**a). The important phase transition for the pnp-switch is the latter, where β-$Ag_{18}Cu_3Te_{11}Cl_3$ – stable between 216 and 288 K – converts to α-$Ag_{18}Cu_3Te_{11}Cl_3$, the phase present above room temperature. Single crystal structure determinations revealed that the symmetry and therefore also the space group does not change and the cell volume increases continuously without a significant volume discontinuity while undergoing the transition (see **Table 1**). While some physical properties, like the total electrical conductivity, increase continuously without any abrupt change in the temperature window around room temperature, the Seebeck coefficient drops significantly right after the β-α phase transition (Figure 2a). The origin of this intriguing Seebeck modulation effect needs to be identified and discussed. In β-$Ag_{18}Cu_3Te_{11}Cl_3$, a triangular arrangement of Te_2 dumbbells (Te8 sites) and additional coordinating Te neighbors (Te7 sites) create an ordered Te 6.3.6.3 net. Right after the phase transition to α-$Ag_{18}Cu_3Te_{11}Cl_3$ at 288 K, we observe emerging disorder in the Te 6.3.6.3 net (Figure 1d). While the net is fully ordered in the β-polymorph, the occurrence of additional Te sites (Te9) in close vicinity to the Te_2 dumbbells can be identified after the transition. Temperature-dependent joint probability density function (jpdf) plots are given in Figure 1e, where the population of the Te9 site close to the dumbbell sites is represented. The distance between Te9 and Te7 (2.96(4) Å at 330 K) is very similar to the dumbbell distance between two Te8 (2.795(7) Å at 330 K), from which we can conclude that a new dumbbell is formed at this position. Temperature-dependent single crystal XRD measurements for α-$Ag_{18}Cu_3Te_{11}Cl_3$ at 330(1), 350(1) and 400(1) K illustrate that the occupation of Te9 increases linearly with temperature, while that of Te8 decreases. The linear fit crosses the x-axis right at the onset of the phase transition. Further details concerning the temperature-dependent structure analysis are summarized in the Supporting Information section.

2.3. Physical Properties and Possible Applications

The most striking feature during this transition is the variation of the thermopower or Seebeck coefficient. $Ag_{18}Cu_3Te_{11}Cl_3$ displays a gigantic drop of the Seebeck coefficient of over 3000 μV K^{-1} (at ≈295 K) followed by an increase of the thermopower by 4500 μV K^{-1} (320 to 360 K) within a small temperature window of only 50 K (see Figure 2a). Such huge thermopower modulations within 50 K of more than 4 mV K^{-1} close to ambient temperature have never been observed before. This feature should enable the utilization of $Ag_{18}Cu_3Te_{11}Cl_3$ in sensors and power applications at room temperature. The previously mentioned materials show changes of only 1400 μV K^{-1} in $Ag_{10}Te_4Br_3$, 750 μV K^{-1} in $AgBiSe_2$, 700 μV K^{-1} in AgCuS, and 400 μV K^{-1} in $Tl_2Ag_{12}Se_7$ during the pnp-switch.[1,4–6] $Ag_{18}Cu_3Te_{11}Cl_3$ is able to create large voltage drops in a temperature window close to room temperature where manifold applications – e.g. solar cells, catalysts, and sensors – operate. Photoluminescence measurements of $Ag_{18}Cu_3Te_{11}Cl_3$ show two Lorentzian emission lines at 1.35 and 1.5 eV, located in the infrared (Figure 2b). Thermal activation and initiation of the pnp-effect are thus possible by light irradiation. This optical behavior may allow the utilization in solar cells since the band gaps are close to the maximal efficiency for single junction solar cells, as defined by the Shockley–Queisser limit (Figure S7, Supporting Information).[11] The material also shows an extremely low thermal diffusivity, which is beneficial for the application of $Ag_{18}Cu_3Te_{11}Cl_3$ as diodes/transistors due to the maintenance of the thermal gradient and therefore the p- and n- regions (Figure 2c). The thermal diffusivity of $Ag_{18}Cu_3Te_{11}Cl_3$ of 0.08 mm^2 s^{-1} is lower than the values of water (0.135 mm^2 s^{-1}) and polymers like polycarbonate (0.148 mm^2 s^{-1}), polyethylene (0.283 mm^2 s^{-1}), and polystyrene (0.137 mm^2 s^{-1}).[12,13] The thermal conductivity does not change significantly between 260 and 380 K and varies around ≈0.14 W m^{-1} K^{-1} (Figure 2c). This very low and rather temperature-independent thermal conductivity of $Ag_{18}Cu_3Te_{11}Cl_3$ is either caused by its excellent phonon scattering capability due to the intrinsic high cation mobility or by diffuson-mediated thermal transport. The latter mechanism has been recently identified and discussed for silver-ion conducting argyrodites.[14] The calculated thermoelectric figure of merit ZT of 10^{-2} at 320 K is rather low due to the poor electrical conductivity (see Figure 2d). Due to possible applications as thin-layer and bulk material we determined the bulk modulus of this compound via high-pressure XRD experiments. Using a 3rd-order Birch–Murnaghan equation of state fit we derived a bulk modulus of 28.2(11) GPa (Figure 2 e,f, and Figure S4 a,b, Supporting Information).[15] This value is slightly higher than the calculated bulk modulus of

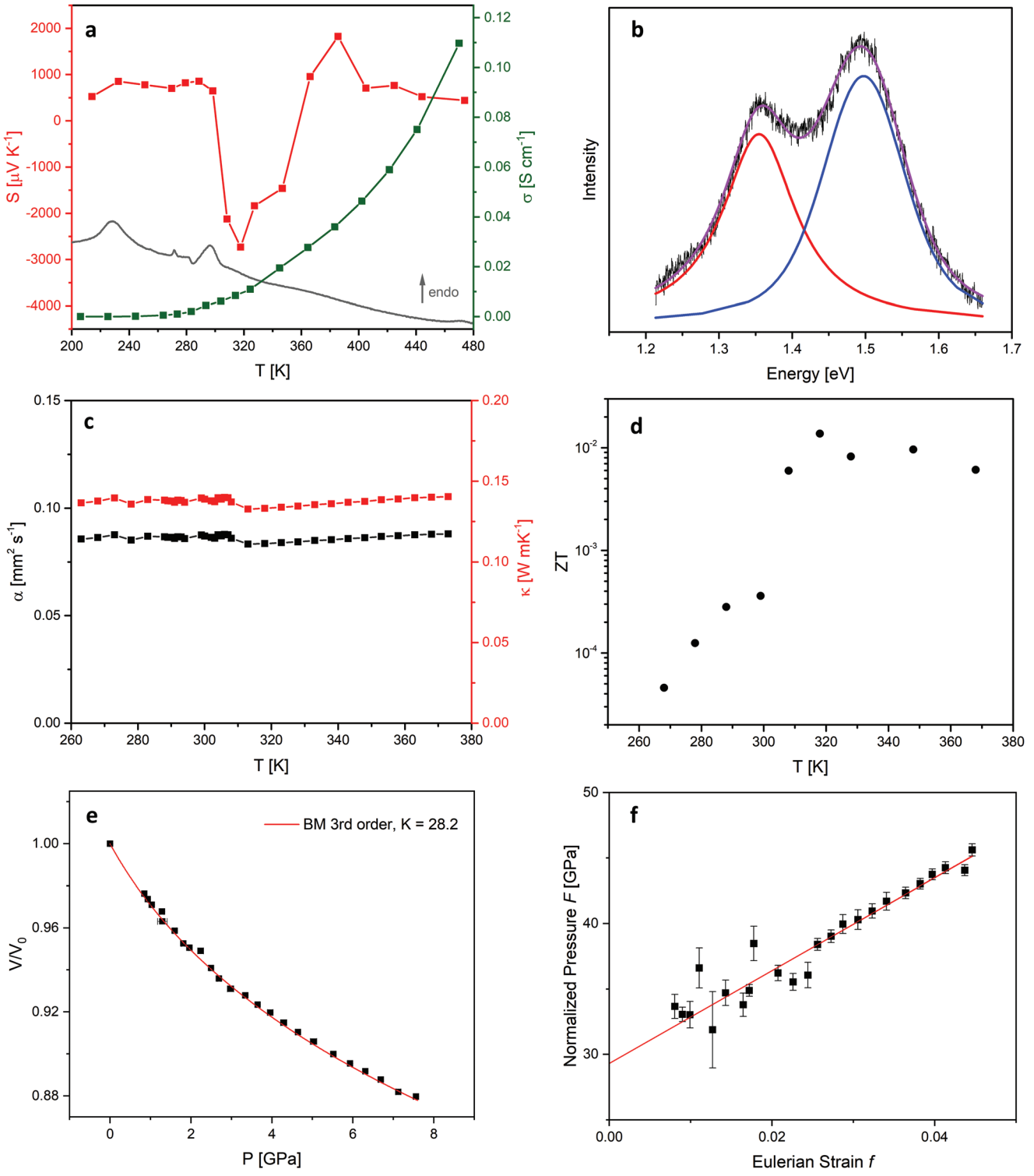

Figure 2. Physical properties of $Ag_{18}Cu_3Te_{11}Cl_3$. a) The Seebeck coefficient (red) varies between 625 µV K^{-1} (298 K) before, and −2731 µV K^{-1} (317 K) and 1824 µV K^{-1} (386 K) directly after the β-α phase transition. DSC (grey) illustrates the reversible endothermic thermal effects at 216(3) and at 288(3) K (onset values, the small effect at 273 K is due to water impurity in liquid nitrogen). The total electrical conductivity (green) varies between 6 mS cm^{-1} (300 K) and 110 mS cm^{-1} (470 K). b) Photoluminescence measurements (black) show Lorentzian emissions at 1.35 (red) and 1.50 eV (blue). c) Thermal conductivities (red) calculated from thermal diffusivity (black) measurements cumulate in very low values of ≈0.14 W m^{-1} K^{-1} around the β-α phase transition. Effective phonon scattering takes place around room temperature. d) Calculated thermoelectric figure of merit *ZT* value of $Ag_{18}Cu_3Te_{11}Cl_3$. The error was estimated to 10%. e) Bulk modulus determination of α-$Ag_{18}Cu_3Te_{11}Cl_3$ from a 3rd-order fit using the Birch–Murnaghan equation of state resulting in K_0 = 28.2(11) GPa and K' = 12.7(8). An *F-f* plot is given in (f).

Table 1. Single crystal XRD data of α- and β-$Ag_{18}Cu_3Te_{11}Cl_3$ at 270, 330, 350, and 400 K.

	β-$Ag_{18}Cu_3Te_{11}Cl_3$	α-$Ag_{18}Cu_3Te_{11}Cl_3$	α-$Ag_{18}Cu_3Te_{11}Cl_3$	α-$Ag_{18}Cu_3Te_{11}Cl_3$
Temperature [K]	270(1)	330(1)	350(1)	400(1)
Refined composition	$Ag_{17.1(3)}Cu_{2.85(6)}Te_{11}Cl_3$	$Ag_{17.2(5)}Cu_{2.87(8)}Te_{11}Cl_3$	$Ag_{17.2(4)}Cu_{2.86(6)}Te_{11}Cl_3$	$Ag_{16.4(5)}Cu_{2.74(9)}Te_{11}Cl_3$
Molar mass [g mol^{-1}]	3537.7	3548.3	3542.4	3455.8
Crystal size [mm]		$0.1 \times 0.05 \times 0.05$		$0.2 \times 0.1 \times 0.1$
Crystal shape/color		block/black		
Crystal system	hexagonal		hexagonal	
Space group	$P6_3/mcm$		$P6_3/mcm$	
Z	6		6	
a [Å]	13.4709(12)	13.5506(12)	13.5651(12)	13.5775(12)
c [Å]	30.818(2)	30.7723(19)	30.8198(12)	30.822(3)
V [Å^3]	4843.1(7)	4893.4(7)	4911.4(6)	4920.7(8)
ρ_{calc} [g cm^{-3}]	7.2777	7.2246	7.186	6.9971
Diffractometer		STOE Stadivari		
Radiation [Å]		0.71073 (Mo $K_{\alpha 1/2}$)		
μ [cm^{-1}]	22.16	21.771	21.656	21.114
F[000]	9061	9089	9074	8847
θ range [°]	3.04 – 30.13	3.01 – 29.99	3 – 30	3 – 29.99
hkl range	−18/ +9, 0/ +9, 0/ +43	−19/ +9, 0/ +19, 0/ +38	−19/ +9, 0/ +19, −43/ +43	−18/ +19, −18/ +19, −43/ +41
No. of reflections	8811	8099	17785	67811
R_{int}	0.0431	0.0613	0.0938	0.1913
Data/parameters	2053 / 275	1736 / 285	2154 / 301	2330 / 308
R / wR [I > 3σ (I)]	0.0375 / 0.0637	0.0370 / 0.0598	0.0378 / 0.0625	0.0370 / 0.0726
R / wR [all]	0.0887 / 0.0794	0.1169 / 0.1169	0.1117 / 0.0839	0.1476 / 0.1238
Goodness of fit	1.23	0.98	1.13	1.12
Res. elec. dens. max / min [e Å^{-3}]	−1.84 / +1.56	−1.47 / +1.26	−1.62 / +0.88	−1.53 / +1.30

Cu_2Te K_0 = 22.9 GPa.[16] We observed no further phase transitions; at room temperature α-$Ag_{18}Cu_3Te_{11}Cl_3$ maintains the same structure up to ≈8 GPa.

2.4. Mechanism of the pnp-Switch

An important point to elucidate is the mechanism of the pnp-transition in $Ag_{18}Cu_3Te_{11}Cl_3$. The Seebeck coefficient is defined by the Mott equation:[17,18]

$$S = -\frac{\pi^2}{3}\frac{k_B^2 T}{e}\left[\frac{1}{n}\frac{dn(E)}{dE} + \frac{1}{\mu}\frac{d\mu(E)}{dE}\right]_{E=E_F} \quad (1)$$

where S, k_B, e, n, and μ are the Seebeck coefficient, Boltzmann constant, electron charge, charge carrier concentration, and carrier mobility, respectively. This equation may be understood as the partial derivative of the density of states (DOS) analyzed at the Fermi energy. As such, changes in the magnitude and signal of the Seebeck coefficient represent variation in the local state of the DOS at E_F. Two effects in $Ag_{18}Cu_3Te_{11}Cl_3$ are responsible for such modulation of the DOS and the resulting pn-switch that occurs right after the β-α phase transition. One is localized in the heaviest atom (Te) substructure, and the other in the d^{10} cation substructure. The effect in the Te substructure can be regarded as a local 2D charge density wave (CDW) within the 6.3.6.3 Te kagomé net. The disorder phenomenon and the occupancy of additional Te sites within the kagomé net lead to significant atomic rearrangements and charge fluctuations. In **Figure 3**a, the proposed mechanism of the atomic rearrangement in the Te 6.3.6.3 net is illustrated. A partial local rearrangement of Te_2 dumbbells causes the observed variation in occupancy of Te8 and Te9 sites in the kagomé net. The Te_2 dumbbell – which is fully localized in β-$Ag_{18}Cu_3Te_{11}Cl_3$ – is shifted toward the corners of the Te triangle (see Figure 3a) within the kagomé net. This dynamic rearrangement is only possible through internal redox processes with charge fluctuation. Electron delocalization and transport are thus enabled via this dynamic process within the Te substructure in α-$Ag_{18}Cu_3Te_{11}Cl_3$. The temporary excess of free electrons leads to an upward shift of the Fermi level. As even small amounts of free electrons have a considerable impact on the electron-hole balance in semiconductors, the temporary availability of electrons leads to pn-switching during the phase transition. The observed broad Seebeck modulation and drop – in comparison to the other known pnp-compounds – might be explained by the continuous temperature-driven

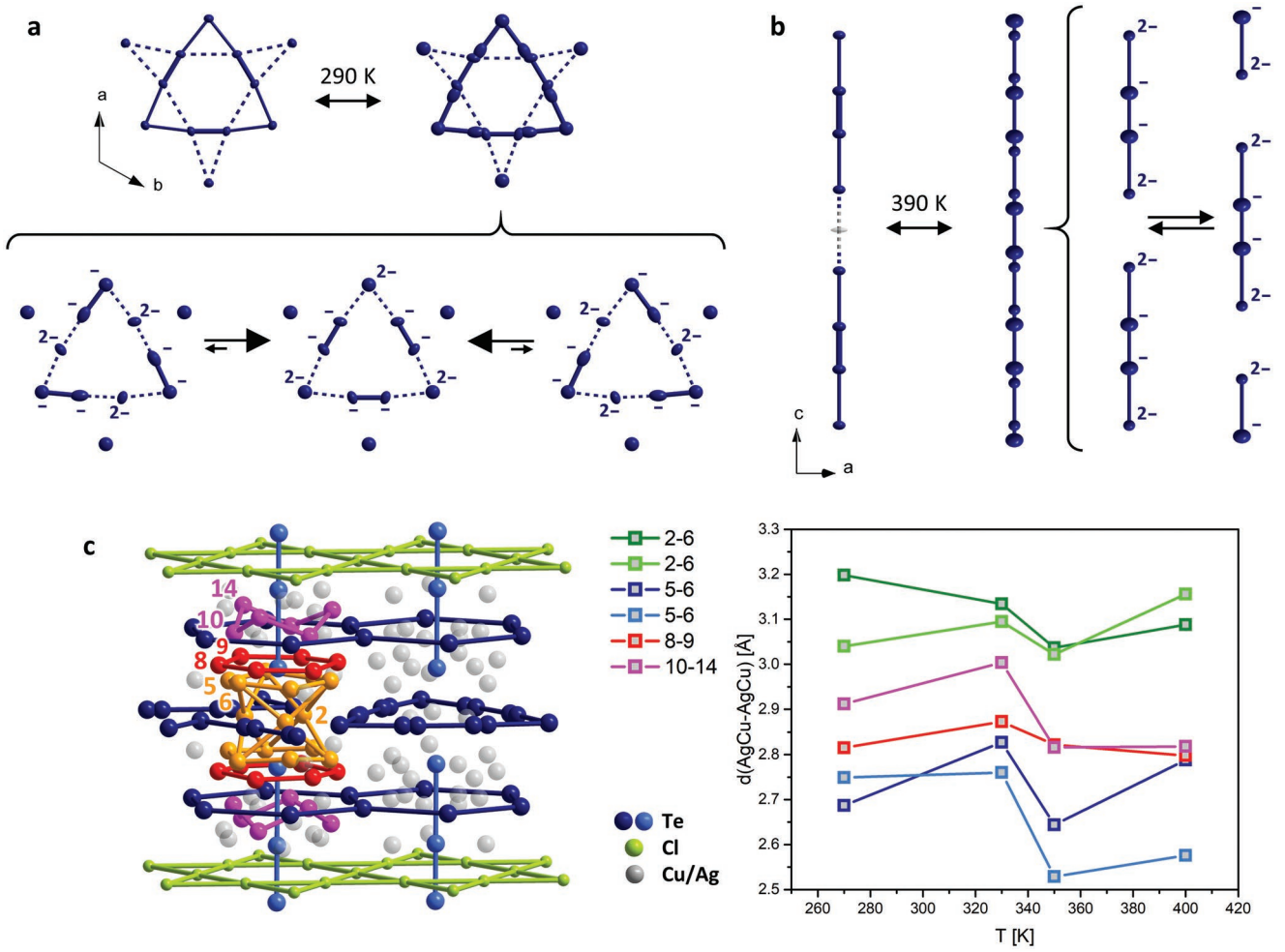

Figure 3. Mechanism of pnp-switching. a) Structure sections of Te 6.3.6.3 in β- and α-$Ag_{18}Cu_3Te_{11}Cl_3$. Proposed mechanism of dumbbell rearrangement in α-$Ag_{18}Cu_3Te_{11}Cl_3$. b) Structure sections of the isolated Te_4 strands and the equidistant Te chain that is formed during the β- to α-$Ag_{10}Te_4Br_3$ phase transition. c) Mixed occupied Ag/Cu sites in $Ag_{18}Cu_3Te_{11}Cl_3$. d^{10}-d^{10} interactions in the coinage metal substructure shorten the coinage metal distances. After the β-α phase transition, the d^{10} ions interact with each other and show reduced bond distances upon heating. Four different cation site couples are selected to illustrate this phenomenon, and their bond lengths are given as a function of temperature. Ag/Cu bond distances are defined by the maxima of electron density derived from the so-called mode positions, which were identified after the integration of the probability density functions of non-harmonically refined displacements for each ion.

occupation of the Te9 site that is necessary to induce the pn-transition.[1,4–6] A comparable mechanism of atomic rearrangements in the Te substructure can be found in pnp-switching $Ag_{10}Te_4Br_3$. In this case, the rearrangement of strands of Te_4 units leads to a 1D CDW. The reorganization from a strand of oligomeric Te_4 units to a dynamically disordered equidistant Te-chain (shown in Figure 3b) occurs in a similar manner via internal redox processes. This phenomenon in $Ag_{10}Te_4Br_3$ also allows the delocalization of electrons along the equidistant Te chain and the temporary generation of extra conduction electrons in higher band states, resulting in an upward shift of the Fermi level, and consequently causing the observed pn-switching after the phase transition temperature of 390 K. In the $Ag_{10}Te_4Br_3$ high-temperature α-polymorph, the mobility within the Te-strands becomes too high to enable constructive delocalization of electrons and therefore the system switches back to p-type conduction.[1]

In $Ag_{18}Cu_3Te_{11}Cl_3$ a partial 2D CDW occurs. According to our single crystal structure determination data, we see a temperature-dependent population of an additional Te site (Te9) at the onset of the β-α phase transition (Figure 1e). The population increases linearly with temperature up to 28.5% at 400 K, which is a clear indicator of a dynamic process instead of a static disorder.

To further investigate this phenomenon, ^{125}Te solid-state MAS NMR experiments were acquired at various temperatures (**Figure 4**a). As reported previously, the isolated Te^{2-} ions are located in the chemical shift range between 1600 and 1900 ppm (referenced to $(CH_3)_2Te$), while resonances for the polytelluride $[Te_n]^{m-}$ units in the kagomé net occur at chemical shifts ranging from 600 to 900 ppm.[1,19] These atoms are also characterized by a much larger chemical shift anisotropy (≈800 ppm vs 300 ppm for the isolated species) due to the anisotropic environment originated by the Te—Te bond. The resonances between

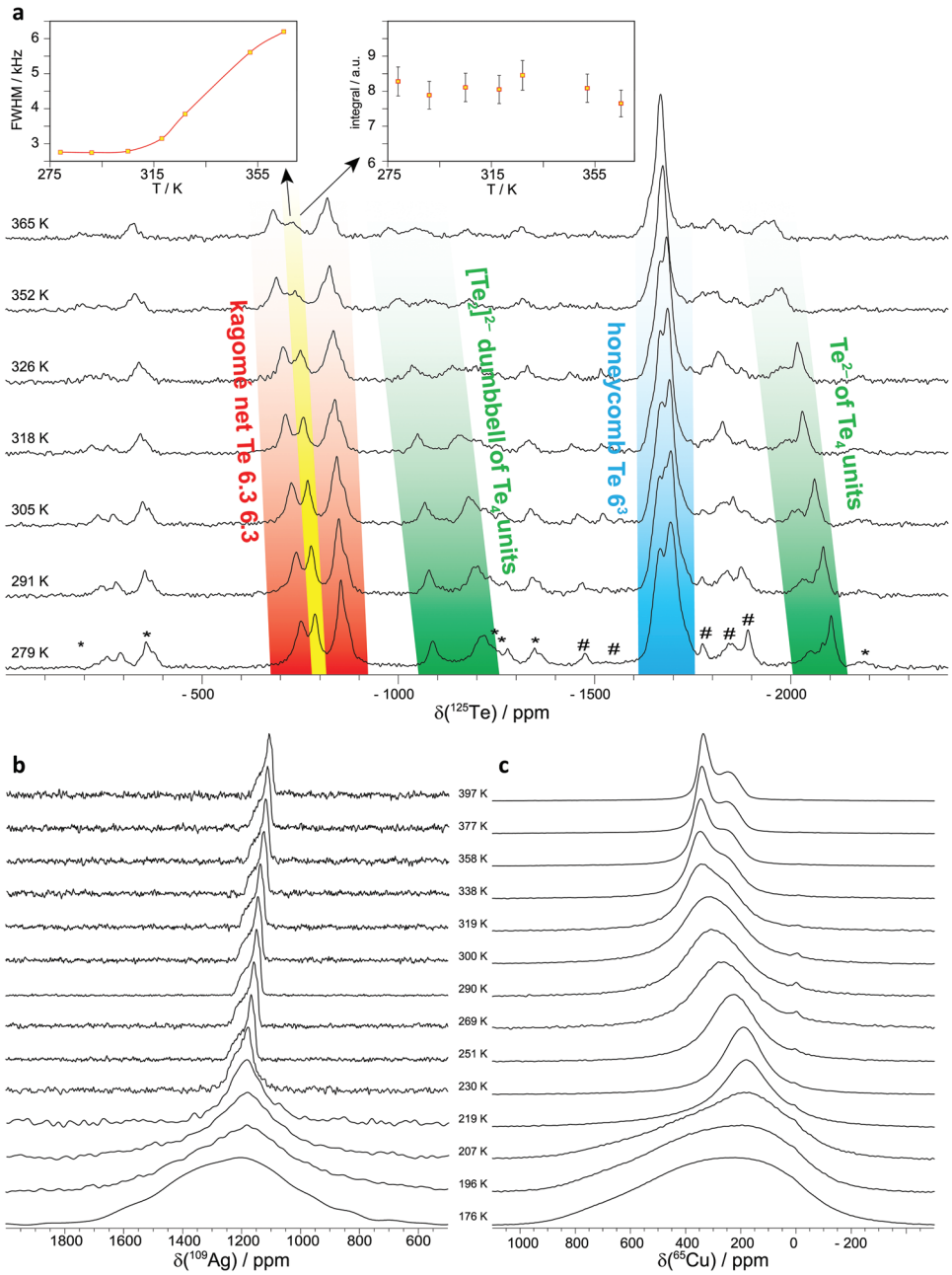

Figure 4. Solid-state NMR spectra of $Ag_{18}Cu_3Te_{11}Cl_3$ at different temperatures. a) ^{125}Te MAS spectra with color-coded assignment of the characteristic Te subunits. The resonance where coalescence occurs is marked in yellow. The corresponding typical trends for the full width at half maximum (FWHM) and integral for this resonance are given in the insets. The asterisks marks spinning sidebands and the hashtags the impurities. b) ^{109}Ag and c) ^{65}Cu static spectra.

1000 and 1200 ppm as well as the ones between 1900 and 2100 ppm could be assigned to the atoms in Te_4 units, the former corresponding to the $[Te_2]^{2-}$ dumbbells and the latter to the Te^{2-} of the Te_4 units. Except for the isolated Te^{2-} within the honeycomb layer (1600 to 1800 ppm), all the other ^{125}Te resonances shift downfield significantly with increasing temperature (Figure 4a; Figure S5a, Supporting Information). Within the group of resonances assigned to the kagomé net (700 to 900 ppm), the Te atoms drifting the most are the ones at 750 and 790 ppm. In addition, the amplitude of the change with temperature for the resonance at 790 ppm is particularly striking. While constant below 315 K, its full width at half maximum (FWHM), almost doubles while retaining the overall integral up to 365 K. This behavior is characteristic of the onset of a coalescence phenomenon under MAS conditions.[20] For a ^{125}Te enriched sample, we observed that the magnitude of the chemical shift anisotropy (CSA) for the same resonance (see Figure S5b, Supporting Information) decreases within the same temperature range, supporting the hypothesis of coalescence. This phenomenon substantiates the onset of dynamic

disorder of the Te atoms within the kagomé net with correlation times on the order of tens of kHz. The disorder corresponds to a chemical exchange between isolated Te^{2-} atoms and $[Te_2]^{2-}$ dumbbells as suggested by the diffraction data (Figure 1e). As the onset temperature for the dynamic exchange coincides with the initiation of the pnp-switch, both effects are likely linked.

Temperature-dependent XRD and ^{109}Ag and ^{65}Cu solid-state NMR data suggest that the pnp-switch is also connected to changes in the dynamic disorder of the d^{10} ion substructure. The first phase transition observed at 216(3) K is accompanied by a pronounced narrowing of the ^{109}Ag and ^{65}Cu resonances (Figure 4b,c). Thus, above 220 K, both cations exhibit fast motion. The remaining narrow shape for the ^{109}Ag NMR spectra, typical for an almost axially symmetric chemical shift anisotropy, is in line with a restriction of the ion mobility in two dimensions parallel to the (001) layer.[21] Diffraction data suggest that silver and copper are mixed within these layers. Nevertheless, the presence of two resonances at 1160 and 1164 ppm in the ^{109}Ag MAS NMR spectrum, at chemical shifts comparable to similar compounds, suggests two slightly different environments in the cation layers.[1]

In contrast to the lineshape of the ^{109}Ag NMR spectra, which is temperature-independent above 270 K, the lineshape of the ^{65}Cu NMR signal in the temperature range of the pnp-switch is temperature-dependent and even develops an anisotropic shape (quadrupolar and chemical shift interaction) toward higher temperatures. This effect is most likely caused by the attraction of the silver and copper ions right after the β-α phase transition, as also indicated by the drop in bond lengths between the d^{10} ions observed in temperature-dependent single crystal structure determinations at 270, 330, 350, and 400 K (Figure 3c). Usually, bond lengths tend to extend upon temperature increase; instead, we see a significant decrease upon heating. This effect may tune the Seebeck coefficient as already shown for Ag_5Te_2Cl, a system in which d^{10}-d^{10} interactions were identified as the only source for thermopower modulations.[22] The occurrence of lineshape changes only in the ^{65}Cu resonance suggests a drastic additional change in the Cu mobility around the room temperature β-α phase transition and the consequently stronger d^{10}-d^{10} interactions in the copper sub-ensemble. As discussed earlier on, this feature should also contribute to the modulation of the DOS close to the Fermi level. The sum of both discussed aspects causes the enormous Seebeck coefficient drop, with an unprecedented intensity of 4,500 mV K^{-1}.

2.5. The Position-Independent, Switchable One-Component Diode

The most intriguing property of $Ag_{18}Cu_3Te_{11}Cl_3$ is the pnp-switch at room temperature. It may allow the generation of diodes and transistors by a simple change of temperature. In order to verify the diode behavior of $Ag_{18}Cu_3Te_{11}Cl_3$, we investigated the system at two different temperature conditions and setups. A crystal was mounted onto gold pads with metallic indium so that both ends of the sample are contacted (see **Figure 5**a,b). The first setup was chosen so that the system operates in the β-$Ag_{18}Cu_3Te_{11}Cl_3$ phase, slightly below room temperature. The second setup includes a temperature gradient to bring the system into the pn-transition regime, already in the α-$Ag_{18}Cu_3Te_{11}Cl_3$ phase. Here we used a 295 to 308 K gradient where the hot side is supposedly n- and the cold side p-conducting.

At 283 K we find a linear U/I curve upon polarization between ±1.5 V (Figure 5c). The absence of a Schottky diode behavior indicates that the indium contact is ohmic. After unilaterally increasing the temperature, we were able to apply a temperature gradient of 308 to 295 K to the crystal. Now, the U/I curve is significantly different. The hot side should transition to the electron-conducting n-phase while, at the opposite end, holes remain as majority carriers, effectively creating a pn-junction across the semiconductor. Indeed, a rectifying behavior can be seen in the U/I curves measured under a temperature gradient, with a forward current over 10 times larger than the reverse current at ±1.0 V, as can be seen in Figure 5c. A junction potential of 0.3 V is determined for the transitory diode. Upon cooling back to 283 K, the system transitions to its starting configuration (the β-phase), and measurements yield the same linear U/I curve as before the application of the gradient. This reversibility clearly rules out the formation of additional semiconducting phases between the indium solder and $Ag_{18}Cu_3Te_{11}Cl_3$ during our measurements upon polarization or temperature treatment. To further substantiate this assumption, we used a different solder material to contact $Ag_{18}Cu_3Te_{11}Cl_3$. Using lead/tin solder we find the same behavior and diode formation as in the case of the indium solder (Figure S6a, Supporting Information).

If U/I measurements are performed isothermally (without an applied, defined temperature gradient) the material behaves ohmically even in the pn-transition range. This observation rules out the formation of a Schottky diode at higher temperatures (299 to 331 K, see Figure 5e). Furthermore, the curves also indicate the absence of effects caused by polarization and mass transport due to the mobile Ag and Cu ions.

These findings substantiate the creation of a thermally-induced single-material pn-junction. Before we step into the discussion, the type of junction that is formed here needs to be addressed and defined. A heterojunction is generated by contacting two dissimilar materials where one is a p- and the other an n-type semiconductor, as is the case of GaAs/GaAlAs lasers. On the other hand, a homojunction is generated by different doping characters in a given material without affecting its structure, such as an n-Si/p-Si junction. As shown earlier, the defect structure of the studied compound varies during the pn-switch but the symmetry and general structural units remain virtually unchanged. Therefore, according to symmetry considerations, the interface between the two phases could be defined as a homojunction. However, regarding the defined property change, the thermal signature in DSC, and the significant changes in defect and electronic structure, the term heterojunction may also partially explain the electronic situation. Neither of the current terms correctly encompasses the real structure of this novel system. Thus, we define a new type of junction, an ambijunction, to illustrate the ambivalent character in this new material.

The switching time of this single crystal diode (forward–reverse direction) has been assessed via the application of

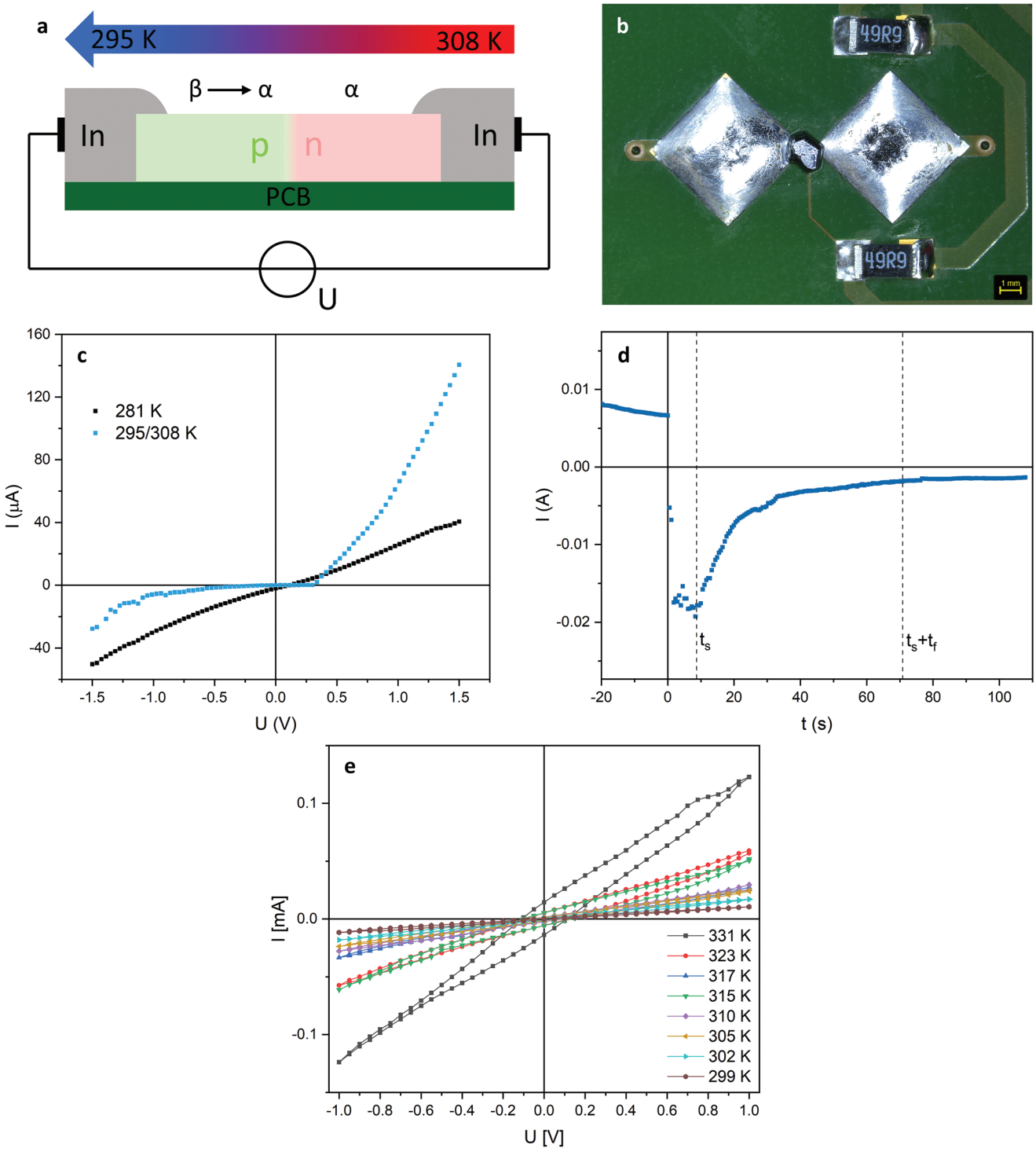

Figure 5. Diode fabrication and *U*/*I* characterization. a) Scheme of the measurement set-up. b) Single crystal of $Ag_{18}Cu_3Te_{11}Cl_3$ mounted on top of Au electrodes and contacted with metallic In. The 49 Ω resistances used to apply a temperature gradient via resistivity heating can be found next to the right contact. c) *U*/*I* plot measured at 281 K within β-$Ag_{18}Cu_3Te_{11}Cl_3$ (black line) and after applying temperature to the system to create a gradient of 13 K between 295(1) and 308(1) K (blue line). d) Switching time of the diode under the same thermal gradient. A 5 V forward was applied, followed by a −5 V reverse current at $t = 0$. The errors of the measured values are located within the points. e) To ensure that no Schottky diode is being formed in the applied temperature ranges, we also measured isothermal *U*/*I* curves for $Ag_{18}Cu_3Te_{11}Cl_3$ up to 331 K. When the entire crystal was held at the same temperature, no rectifying character was found. A conductivity increase was seen at higher temperatures as is expected for a semiconductor. The errors of the measured values are located within the points.

a 5 V forward potential for 60 s to induce the build-up of the minority carrier at the quasi-neutral regions surrounding the junction (Figure 5d). Subsequently, the device was turned off via the application of a reverse −5 V potential. The linear removal of the excess minority carrier leads to a steady current that is much larger than the saturation current of the device. The switching time t_s for the removal of the excess carriers in this system was ≈8.7 s. After this time, the current decays exponentially toward the saturation limit of the device. The fall time t_f – needed to reach 10% of the initial reverse current – was estimated at 62.4 s.

The initiation of this diode effect is determined in our experimental setup as a sum of the time constants of the several different thermal transport phenomena taking place. Heat must be transferred from the resistance via the metallic contact to the sample. This non-optimized process takes a while, generally a few minutes. This aspect of the measurement setup will be optimized in the future. The full inversion of the p- and n-regions in the given experiment can be realized in minutes in this experimental setup for a mm-sized crystal. This secondary switching process (change of direction besides on–off states) may also be optimized by downscaling of the crystals.

The observed switching is a further indication that the thermal gradient successfully induces the creation of a pn-junction, as this is the only likely source for the shape of the current decay displayed by the device. Furthermore, the long times associated with t_s and t_f again rule out the creation of a Schottky diode instead of a true pn-junction, as the operation in the first is associated with majority carriers, which display higher mobilities, leading to very fast switching. These measurements unambiguously illustrate the creation of the first-ever single-material functional pn-junction, without the need for nanostructuring or advanced architectures, as the diode behavior is an intrinsic property of the bulk material itself. In the future, we intend to downscale the device and material size from the mm to the μ meter regime. This will speed up temperature dissipation and operating speed drastically.

The question arises if the pn-junction formation is unique for $Ag_{18}Cu_3Te_{11}Cl_3$. We selected another pnp-switching material, AgCuS, with a higher switching temperature of 364 K to verify if a diode can also be formed for this material. This is indeed the case: in a temperature gradient of 333(1) to 365(1) K, this material also forms a diode at room temperature while its behavior is ohmic. The measurement can be found in Figure S6b (Supporting Information).

2.6. Impact on Electronics and Energy-Related Science

With the simple and defined creation of a working pn-junction and the consequent diode formation, the process in general, and the compound, in particular, have huge application potential in energy-related science. A single-junction solar cell might be realizable, wherein the pn-junction is generated in a certain temperature gradient directly on the device. Such pn-ambijunction formation and the intrinsic charge separation might be a source for effective water splitting purposes, either stand-alone or as a tandem photoelectrochemical (PEC)-thermoelectrical (TE) device.[23] One step further from the position-independent or position-variable diode is the generation of a position-independent bipolar junction transistor (BJT) with a larger gradient also encompassing the other p-conducting temperature region of $Ag_{18}Cu_3Te_{11}Cl_3$. Similarly, a field effect transistor (FET) may be constructed with the application of heat at the source and drain regions, with the channel below the transition temperature. With the appropriate design, a single device could work as a resistance, a diode, or a transistor, depending on the temperature gradient and the position of the connections. A variation of the FET could also be realized where the role of the regular gate is substituted by a thermal gate. The inversion layer at the interface between the channel and gate would be created and controlled by temperature instead of local polarization. Such thermal effect transistor (TET) could also be exploited in the recycling of thermal waste generated in the normal operation of FETs, leading to the creation of even more processing units. Due to the possibility of generating a diode or transistor at the place where it is occasionally needed, a new IT architecture might be possible, not demanding the preparation of different p- and n-doped regions to form rectifying devices, or a pre-adjustment of the architecture to manipulate the charge carrier density by gate biasing.[24–26] Recently AgI was used to program WSe_2 devices that can be reversibly transformed into transistors with reconfigurable carrier types. Homojunctions with switchable polarities were generated using superionic silver iodide as a medium to polarize WSe_2 by van der Waals or dispersive interactions via an ion gradient in AgI. Unfortunately, such a device requires the deposition and alignment of several materials and a high-temperature treatment of 147 °C to reverse the polarization by initiating silver ion conductivity in AgI.[27] Instead, in the case of $Ag_{18}Cu_3Te_{11}Cl_3$, only one material needs to be deposited, and external stimuli that are able to increase the temperature by a few Kelvin may be used to address the necessary junction formation. This junction may either be kept present in a stable temperature gradient or canceled by its removal. The observed effect is also intrinsic to the bulk material, without the need for nanostructuring or complex architectures. The temperature range in which the effect occurs is also very convenient. For comparison, Wu, Wang, and collaborators recently reported superconducting heterostructures, so-called field-free Josephson diodes, with rectifying character.[28] Although impressive, the diode behavior is only observed close to 0 K, hindering the viability of these devices in most practical applications. In our system, the application temperature at ambient conditions is more beneficial and useful.

Another huge field for semiconductors and the utilization of opposite charge carriers is electrocatalysis. Using the described diode formation effect in electrocatalytic reactions can open a wide field of applications. Recently, it has been shown that ultra-thin semiconductors can be used as effective electrocatalysts, although they suffer from low intrinsic carrier concentrations.[29]

3. Conclusion

In this work, the polymorphic compound $Ag_{18}Cu_3Te_{11}Cl_3$, a newly discovered addition to the class of coinage metal chalcogenide halides, was successfully synthesized. The β-α phase

transition takes place close to room temperature, and at the same time enables reversible switching from an n- to p-type semiconductor and back. For the first time, this allows the fabrication of a commercially viable, easily accessible single-material diode. In our case, we are able to generate opposite charge carriers and n- or p-type semiconductor regions in bulk materials by a simple temperature gradient and at positions where opposite charge carriers are needed. With an appropriate setup, electrocatalysis can be initiated where a suitable temperature gradient is provided on one side and the reaction takes place on the opposite side of a thin-layer device. Future optimization in temperature control should enable the realization of a single-material transistor, potentially leading to novel applications and devices. The newly described phenomenon of the temperature gradient-induced, position-independent, and switchable pn-junction should lead to the observation of emergent anomalous effects. Thus, the nascent field of single-material electronic devices begins.

4. Experimental Section

Synthesis: $Ag_{18}Cu_3Te_{11}Cl_3$ was prepared from a stoichiometric mixture of silver (Chempur, 99.999%), copper(I) chloride (Alfa Aesar, 97%), and tellurium (Chempur, 99.999%) on a gram scale. The starting materials were sealed into evacuated silica glass ampules, heated to 1320(1) K, held at this temperature for 3 h, and quenched in an ice bath. The crude product was finely ground and annealed for 7 days at 660(1) K followed by slow cooling to room temperature. This synthesis route led to phase pure black crystalline products.

XRD Experiments: Powder XRD data were collected with a Stoe STADI P powder diffractometer equipped with a position-sensitive Mythen 1K detector using Cu $K_{\alpha 1}$ radiation (λ = 1.54060 Å, curved Ge(111) monochromator). Data analysis was performed using the STOE WinXpow software package.[30] Single crystal XRD measurements were performed at 200(1), 270(1), 330(1), 350(1), and 400(1) K on a Stoe STADIVARI diffractometer fitted with Mo $K_{\alpha 1/2}$ radiation (λ = 0.71073 Å), a Dectris hybrid pixel detector and an Oxford Cryostream plus system. Data reduction was performed using the Stoe X-AREA package.[31] Structures were solved using the charge-flipping algorithm implemented in the Jana 2006 program suite.[32,33] Numerical absorption correction was performed based on an optimized crystal shape derived from symmetry-equivalent reflections. Space groups were determined by careful analysis of Laue symmetry and extinction conditions. While the structure of γ-$Ag_{18}Cu_3Te_{11}Cl_3$ (200 K) was still not solved due to severe twinning, the data for β-$Ag_{18}Cu_3Te_{11}Cl_3$ (270 K) and α- $Ag_{18}Cu_3Te_{11}Cl_3$ (at 330 K, 350 K, and 400 K) were deposited with the Cambridge Structure Database (https://www.ccdc.cam.ac.uk/structures/): CSD 2201919 (270 K); CSD 2201916 (330 K); CSD 2201917 (350 K); CSD 2201918 (400 K)

Thermal Analysis: Phase pure crystalline material was transferred to an aluminum crucible and differential scanning calorimetry (DSC) was performed with a Netzsch DSC 200 F3 Maia device. The measurement was conducted under N_2 atmosphere in the temperature range of 143 to 523 K with a heating–cooling rate of 10 K min^{-1}. The thermal effects were derived from the onset temperatures. Data analysis was performed using the Netzsch Proteus Thermal Analysis software package.[34]

Measurements of Electrical Conductivity and Seebeck Coefficient: Finely ground phase pure $Ag_{18}Cu_3Te_{11}Cl_3$ was pressed under vacuum to a pellet of 13 mm diameter and 1.23 mm thickness reaching 90% of the crystallographic density. The Seebeck coefficient and the electric conductivity were measured simultaneously directly at Netzsch with a Netzsch SBA 458 Nemesis under a continuous helium flow. The electrical conductivity was determined using the four-point probe. The technical measurement error was ±7% for the Seebeck coefficient and ±5% for the electrical conductivity. Data analysis was performed with the Netzsch SBA-measurement software package.[35]

Thermal Diffusivity Measurements: Thermal diffusivity was measured by laser flash analysis (LFA) on an LFA 467 HyperFlash setup (Selb, Germany) in an atmosphere of pure nitrogen. The ignition voltage of the flash lamp was set to 250 V and the pulse width was 600 µs. The hot-pressed pellet with a diameter of 10 mm and a thickness of 2.0 mm was spray-coated with a graphite layer to enhance emissivity. An improved version of the model proposed by Cape and Lehman was employed to calculate the thermal diffusivity.[36,37] Data analysis was performed using the Netzsch Proteus Thermal Analysis software package.[38] Thermal conductivity was obtained from thermal diffusivity measurements using the following equation:

$$\kappa = \alpha \times \rho \times c_p \tag{2}$$

with α = thermal diffusivity of the material, ρ = density of the material, c_p = specific heat capacity, and κ = thermal conductivity. The Dulong–Petit rule was applied to approximate the specific molar heat capacity of the material in the given temperature range of 260 to 380 K.

Photoluminescence Spectroscopy: Photoluminescence spectra were recorded at room temperature using a WITec alpha300R equipped with an Olympus LMPlanFL N 50 × / 0.5 objective. The pressed pellet was irradiated with a 532 nm laser with 0.15 mW and a 300 g mm^{-1} grating. Each measurement was integrated for 30 s with 3 accumulations.

Solid-State NMR: In order to reduce measuring time for solid-state ^{125}Te NMR spectroscopy, $Ag_{18}Cu_3Te_{11}Cl_3$ using enriched ^{125}Te (STB Isotope Germany, ^{125}Te content 94%) was prepared. The crude ^{125}Te powder was purified in a hydrogen stream at 673 K to remove traces of tellurium oxide. The same synthesis protocol reported earlier on was followed, taking the different molecular weights of the enriched ^{125}Te into account.

^{125}Te MAS NMR experiments were carried out on a Bruker 400 Avance III HD spectrometer (B_0 = 9.4 T) working at a ^{125}Te frequency of 126.1 MHz. The samples were confined in the middle third of the rotor to minimize temperature gradients and were spun at 62.5 kHz using a Bruker double resonance 1.3 mm MAS probe. The single-pulse MAS spectra were obtained after a 90° pulse of 0.95 µs with recycling delays of 0.5 – 4.0 s. ^{125}Te was referenced to $(CH_3)_2Te$, using $Te(OH)_2$ as a secondary reference. The chemical shift anisotropies were extracted from the profiles of the MAS spectra using TopSpin 3.6.3. ^{109}Ag and ^{65}Cu were acquired on a Bruker 600 Avance III HD spectrometer (B_0 = 14.1 T) working at 28.0 and 170.5 MHz for ^{109}Ag and ^{65}Cu, respectively. For ^{109}Ag and ^{65}Cu MAS experiments, the samples were spun at 40.0 and 62.5 kHz, using a Bruker 1.3 mm double resonance probe. ^{109}Ag single-pulse experiment was acquired after a 90° pulse of 5.5 µs and a recycle delay of 2.0 s. ^{65}Cu MAS spectra were obtained using a rotor-synchronized spin-echo experiment with a 90° pulse of 1.2 µs and a recycle delay of 10 ms. ^{109}Ag and ^{65}Cu static experiments were acquired with a triple-resonance wideline probe using a spin echo experiment with 90° pulses of 7.5 and 2.1 µs, respectively, and echo delays of 40 and 10 µs, respectively. Recycle delays ranged from 5 to 300 s for ^{109}Ag and from 5 to 20 ms for ^{65}Cu. ^{109}Ag was referenced to $AgNO_3$ solution and ^{65}Cu to powdered CuCl. All temperatures were calibrated using $Pb(NO_3)_2$.

Diode Measurements: A single crystal was mounted onto a printed circuit board (PCB) with the aid of indium (Alfa Aesar, 99.999%) or tin/lead (Stannol, composition Sn:Pb:Cu = 60:39:1 wt.%) contacts (Figure 5a,b). To apply a temperature gradient to the crystal, two 49 Ω resistances were placed next to one of the In contacts to create localized heating on one side of the mounted crystal and thus induce a temperature gradient across the device.

β-$Ag_{18}Cu_3Te_{11}Cl_3$: Measurements were conducted inside a refrigerator set to 281(1) K, to start the experiment safely within the β-$Ag_{18}Cu_3Te_{11}Cl_3$ phase. This temperature was chosen to be also in a certain thermal distance to the β-α phase transition. A temperature gradient of 295 to 308 K was applied to the sample by using an external current passing through the 49 Ω resistances. The external current was supplied by a QJE PS6005 switching power supply.

AgCuS: For AgCuS the isothermic temperature point was room temperature (298(1) K) and the temperature gradient of 333(1) to 365(1) K was generated using the aforementioned procedure.

Temperature was controlled by an external thermocouple (RSpro Thermometer device, Ni/Cr/Ni type thermocouple, accuracy ±1K) at the contacts during the measurements. Conductivity measurements were performed using a Keithley 2450 SourceMeter. Voltage errors are ±0.015% and current errors are ±0.03%. This digital multimeter was operated with the aid of KickStart *I–V* Characterizer App. Measurements were performed at a scanning speed of 0.06 V s^{-1}. Data analysis was performed with the Keithley Kickstart *I–V* Characterizer App software package.[39]

Semi-Quantitative Phase Analyses: Energy dispersive X-ray spectroscopy (EDX) was performed using a JOEL JCM-6000 NeoScop with an integrated JOEL JED-2200 EDX unit. The acceleration voltage was set to 15 kV. The EDX results were averaged from at least three different points, selected randomly on the crystal surface. The samples were fixed on a graphite holder with a conductive adhesive polymer tape from PLANO GmbH. More details in the Supporting Information section.

Bulk Modulus Determination: Pressure-dependent determinations of the $Ag_{18}Cu_3Te_{11}Cl_3$ cell parameters were conducted at the I15 beamline at Diamond light source, Ditcot, Great Britain. The applied X-ray wavelength was set to λ = 0.4246 Å. A LeToullec-style membrane diamond anvil cell was used to apply pressure in the range from ambient to 8 GPa. The diamond anvils had 300-micron culets and the gasket material was rhenium. Ruby was used as the internal pressure calibration standard and daphne oil was used as a pressure transmitting medium.[40] Ruby fluorescence was measured with a laser system, and the diffractometer raw data were transferred into a processable format with DAWN.[41] The pressure of each data point was measured by collecting ruby spectra before and after the XRD measurement. A pressure equilibration time of 10 min was applied prior to the pressure and XRD data acquisition. A peak fitting routine with Pseudo-Voigt profiles embedded in the FITYK software suite was used to achieve exact pressure data.[42] XRD data were refined using the JANA 2006 program suite.[33] The determined cell parameters at ambient pressure were used as starting model. A LeBail fitting routine, a Legendre polynomial function with 18 background parameters, and a Pseudo-Voigt profile were used to refine the XRD data profile. Cell parameters were determined for each data point with an unrestricted refinement of the cell parameters. The space group $P6_3/mcm$ determined at ambient pressure was applied in the entire pressure range. No change in symmetry in this pressure regime was detected. For each new cell refinement, the previous cell parameters were used as a starting model. Data after the cell parameter refinements are summarized in Table S18 (Supporting Information).

The acquired pressure data was fitted with a Birch–Murnaghan equation of state (EoS):[15]

$$P=\frac{3}{2}K_0\left[\left(\frac{V}{V_0}\right)^{-\frac{7}{3}}-\left(\frac{V}{V_0}\right)^{-\frac{5}{3}}\right]\left\{1+\frac{3}{4}(K'-4)\left[\left(\frac{V}{V_0}\right)^{-\frac{2}{3}}-1\right]\right\} \quad (3)$$

with P = applied pressure in GPa, K_0 = bulk modulus in GPa, K' = pressure derivate of bulk modulus, V_0 = cell volume at ambient pressure in Å^3, and V = cell volume at a given pressure P in Å^3 to determine the bulk modulus K_0. The software EoSFit7c was used for the fitting.[43]

Using the cell volume at ambient pressure of V_0 = 4898(4) Å^3, which was determined by single crystal structure determination experiments, values of K_0 = 28.2(11) GPa and K' = 12.7(8) from a 3rd-order EOS fit was calculated. In order to verify the significance of the fit the Eulerian strain f:

$$f=\frac{1}{2}\left[\left(\frac{V}{V_0}\right)^{-\frac{2}{3}}-1\right] \quad (4)$$

was plotted against the normalized pressure F:

$$F=\frac{P}{3f\times(1+2f)^{\frac{5}{2}}} \quad (5)$$

which is shown in Figure 2f. According to the *F-f* plot values of K_0 = 29.3 GPa and K' = 12.1 were found. The *F-f* plot substantiates the significance of K' in the EOS which significantly deviates from a 2nd-order representation of K' = 4. More details are in the Supporting Information section in chapter 3.

[CCDC 2201916/2201917/2201918 /2201919 contains the supplementary crystallographic data for this paper. These data can be obtained free of charge from The Cambridge Crystallographic Data Centre via www.ccdc.cam.ac.uk/data_request/cif.]

Supporting Information

Supporting Information is available from the Wiley Online Library or from the author.

Acknowledgements

A.V., A.R., and P.D. contributed equally to this work. The authors thank Dr. Ekkehard Post from Netzsch, Selb, Germany for the temperature-dependent measurement of the Seebeck coefficient, and the electric conductivity on their in-house equipment and Sylvio Richter from InfraTec, Dresden, Germany for high-resolution IR camera measurements. The conduction of EDX measurements by Katia Rodewald at the Wacker Chair of Macromolecular Chemistry, TUM, is gratefully acknowledged. A.V., A.R., P.D., and R.S. thank the TUM Graduate School for their support. J.V. thanks for a stipend founded by the TUM Talent Factory program. Funded by the Deutsche Forschungsgemeinschaft (DFG, German Research Foundation) under Germany's Excellence Strategy EXC 2089/1-390776260. The authors also thank Diamond Light Source, UK, for the provision of beamtime at beamline I15 under proposal number CY30094.

Open access funding enabled and organized by Projekt DEAL.

Conflict of Interest

The authors declare no conflict of interest.

Data Availability Statement

The data that support the findings of this study are available from the corresponding author upon reasonable request.

Keywords

coinage metals, diodes, ion conductors, pnp-switches, polymorphism

Received: September 21, 2022
Revised: October 11, 2022
Published online: November 24, 2022

[1] T. Nilges, S. Lange, M. Bawohl, J. M. Deckwart, M. Janssen, H.-D. Wiemhöfer, R. Decourt, B. Chevalier, J. Vannahme, H. Eckert, R. Weihrich, *Nat. Mater.* **2009**, *8*, 101.
[2] S. Lange, T. Nilges, *Chem. Mater.* **2006**, *18*, 2538.

[3] S. Lange, M. Bawohl, D. Wilmer, H.-W. Meyer, H.-D. Wiemhöfer, T. Nilges, *Chem. Mater.* **2007**, *19*, 1401.
[4] C. Xiao, X. Qin, J. Zhang, R. An, J. Xu, K. Li, B. Cao, J. Yang, B. Ye, Y. Xie, *J. Am. Chem. Soc.* **2012**, *134*, 18460.
[5] S. N. Guin, J. Pan, A. Bhowmik, D. Sanyal, U. V. Waghmare, K. Biswas, *J. Am. Chem. Soc.* **2014**, *136*, 12712.
[6] Y. Shi, A. Assoud, C. R. Sankar, H. Kleinke, *Chem. Mater.* **2017**, *29*, 9565.
[7] J. Peters, O. Conrad, B. Bremer, B. Krebs, *Z. Anorg. Allg. Chem.* **1996**, *622*, 1823.
[8] L. Pauling, *The Nature of the Chemical Bond*, 3rd ed., Cornell University Press, Ithaca, NY **1960**.
[9] A. Vogel, T. Nilges, *Inorg. Chem.* **2021**, *60*, 15233.
[10] A. Vogel, T. Miller, C. Hoch, M. Jakob, O. Oeckler, T. Nilges, *Inorg. Chem.* **2019**, *58*, 6222.
[11] W. Shockley, H. J. Queisser, *J. Appl. Phys.* **1961**, *32*, 510.
[12] D. W. James, *J. Mater. Sci.* **1968**, *3*, 540.
[13] X. Zhang, M. Fujii, *Polym. Eng. Sci.* **2003**, *43*, 1755.
[14] T. Bernges, R. Hanus, B. Wankmiller, K. Imasato, S. Lin, M. Ghidiu, M. Gerlitz, M. Peterlechner, S. Graham, G. Hautier, Y. Pei, M. R. Hansen, G. Wilde, G. J. Snyder, J. George, M. T. Agne, W. G. Zeier, *Adv. Energy Mater.* **2022**, *12*, 2200717.
[15] F. Birch, *Phys. Rev.* **1947**, *71*, 809.
[16] S. Hasan, P. Adhikari, K. Baral, W.-Y. Ching, *AIP Adv.* **2020**, *10*, 75216.
[17] Q. Yang, J. Lee, B. Feng, Y. Ikuhara, G. Kim, H. J. Cho, H. Jeen, H. Ohta, *ACS Appl. Electron. Mater.* **2020**, *2*, 2250.
[18] M. Cutler, N. F. Mott, *Phys. Rev.* **1969**, *181*, 1336.
[19] K. J. D. MacKenzie, M. E. Smith, *Multinuclear Solid-State Nuclear Magnetic Resonance of Inorganic Materials*, Pergamon, Oxford, UK **2002**.
[20] A. D. Bain, *Prog. Nucl. Magn. Reson. Spectrosc.* **2003**, *43*, 63.
[21] C. D. Keenan, M. M. Herling, R. Siegel, N. Petzold, C. R. Bowers, E. A. Rössler, J. Breu, J. Senker, *Langmuir* **2013**, *29*, 643.
[22] T. Nilges, O. Osters, M. Bawohl, J.-L. Bobet, B. Chevalier, R. Decourt, R. Weihrich, *Chem. Mater.* **2010**, *22*, 2946.
[23] J.-Y. Jung, D. Woong Kim, D.-H. Kim, T. Joo Park, R. B. Wehrspohn, J.-H. Lee, *Sci. Rep.* **2019**, *9*, 9132.
[24] D. Li, M. Chen, Z. Sun, P. Yu, Z. Liu, P. M. Ajayan, Z. Zhang, *Nat. Nanotechnol.* **2017**, *12*, 901.
[25] R. Cheng, F. Wang, L. Yin, Z. Wang, Y. Wen, T. A. Shifa, J. He, *Nat. Electron.* **2018**, *1*, 356.
[26] J.-W. Chen, S.-T. Lo, S.-C. Ho, S.-S. Wong, T.-H.-Y. Vu, X.-Q. Zhang, Y.-D. Liu, Y.-Y. Chiou, Y.-X. Chen, J.-C. Yang, Y.-C. Chen, Y.-H. Chu, Y.-H. Lee, C.-J. Chung, T.-M. Chen, C.-H. Chen, C.-L. Wu, *Nat. Commun.* **2018**, *9*, 3143.
[27] S.-J. Lee, Z. Lin, J. Huang, C. S. Choi, P. Chen, Y. Liu, J. Guo, C. Jia, Y. Wang, L. Wang, Q. Liao, I. Shakir, X. Duan, B. Dunn, Y. Zhang, Y. Huang, X. Duan, *Nat. Electron.* **2020**, *3*, 630.
[28] H. Wu, Y. Wang, Y. Xu, P. K. Sivakumar, C. Pasco, U. Filippozzi, S. S. P. Parkin, Y.-J. Zeng, T. McQueen, M. N. Ali, *Nature* **2022**, *604*, 653.
[29] Y. He, Q. He, L. Wang, C. Zhu, P. Golani, A. D. Handoko, X. Yu, C. Gao, M. Ding, X. Wang, F. Liu, Q. Zeng, P. Yu, S. Guo, B. I. Yakobson, L. Wang, Z. W. Seh, Z. Zhang, M. Wu, Q. J. Wang, H. Zhang, Z. Liu, *Nat. Mater.* **2019**, *18*, 1098.
[30] Stoe, *WinXPOW*, Stoe & Cie GmbH, Darmstadt, Germany, **2011**.
[31] Stoe, *X-AREA*, Stoe & Cie GmbH, Darmstadt, Germany, **2015**.
[32] L. Palatinus, G. Chapuis, *J. Appl. Crystallogr.* **2007**, *40*, 786.
[33] V. Petrıcek, M. Dušek, L. Palatinus, *The Crystallographic Computing System*, Institute of Physics, Praha, Czech Republic **2006**.
[34] Netzsch GmbH, *Proteus Thermal Analysis*, Netzsch Gerätebau GmbH, Selb, Germany **2010**.
[35] Netzsch GmbH, *NetzschSBA-Measurement*, Netzsch Gerätebau GmbH, Selb, Germany **2016**.
[36] J. A. Cape, G. W. Lehman, *J. Appl. Phys.* **1963**, *34*, 1909.
[37] J. Blumm, J. Opfermann, *High Temp.-High Pressures* **2002**, *34*, 515.
[38] Netzsch GmbH, *Proteus LFA Analysis*, Netzsch Gerätebau GmbH, Selb, Germany **2021**.
[39] Keithley Instruments LLC, *Kickstart I-V Characterizer App*, Tektronix Inc., Beaverton, United States, **2021**.
[40] K. Syassen, *High Pressure Res.* **2008**, *28*, 75.
[41] J. Filik, A. W. Ashton, P. C. Y. Chang, P. A. Chater, S. J. Day, M. Drakopoulos, M. W. Gerring, M. L. Hart, O. V. Magdysyuk, S. Michalik, A. Smith, C. C. Tang, N. J. Terrill, M. T. Wharmby, H. Wilhelm, *J. Appl. Crystallogr.* **2017**, *50*, 959.
[42] M. Wojdyr, *J. Appl. Crystallogr.* **2010**, *43*, 1126.
[43] R. J. Ross, M. Alvaro, J. Gonzalez-Platas, *Z. Kristallogr. Cryst. Mater.* **2014**, *229*, 405.